fishes

MDPI

Article

Preliminary Sea-Caught Versus Farmed Collection-Source Discrimination of Large Yellow Croaker Using Hyperspectral Features of Anatomical Regions

Xinyu Ai [1,2], Junjie Wu [1], Shengmao Zhang [1,*], Na Lin [1], Banghong Wei [1,3] and Quanyou Guo [1,*]

[1] East China Sea Fisheries Research Institute, Chinese Academy of Fishery Sciences, Shanghai 200090, China; 15937343001@163.com (X.A.); wujj@ecsf.ac.cn (J.W.); linna903368043@163.com (N.L.); weibh@ecsf.ac.cn (B.W.)
[2] School of Information Science and Technology, Dalian Ocean University, Dalian 116023, China
[3] Qingdao Marine Science and Technology Center, Qingdao 266237, China
* Correspondence: zhangsm@ecsf.ac.cn (S.Z.); guoqy@ecsf.ac.cn (Q.G.)

Abstract

Large yellow croaker (*Larimichthys crocea*) is an economically important marine fish, yet rapid and non-destructive discrimination between sea-caught and farmed collection-source groups remains challenging. This study developed a fish-level analytical workflow integrating YOLO11n-seg instance segmentation with visible–near-infrared hyperspectral imaging to extract relative reflectance ratios from six anatomical regions. The analytical cohort comprised 258 unique fish, including 171 sea-caught and 87 farmed individuals. Source categories were assigned according to the original capture or cage-culture collection channels. Fish identity was used as the grouping unit in five-fold internal cross-validation, and classification performance was evaluated based on out-of-fold fish-level predictions. Logistic-regression models achieved AUC values ranging from 0.985 to 1.000 across the six individual anatomical regions. The combined six-region model achieved an accuracy of 0.996 (95% CI, 0.988–1.000) and an AUC of 1.000 (95% CI, 1.000–1.000) within the present cohort. For anatomical-region segmentation, the 20-image validation set contained 140 annotated instances. Bounding-box precision, recall, mAP@0.5, and mAP@0.5–0.95 were 0.976, 0.983, 0.981, and 0.700, respectively, while the corresponding mask metrics were 0.969, 0.976, 0.972, and 0.669. These results indicate that region-specific hyperspectral information can support highly accurate internal discrimination between the two collection-source groups and provide an interpretable basis for characterizing source-associated spectral differences. However, the source labels were not independently verified, potentially influential covariates were incompletely recorded, and no independent external cohort was available. Therefore, the present findings should be interpreted as internally validated collection-source discrimination rather than verified provenance authentication or evidence of external generalizability.

Keywords: large yellow croaker; hyperspectral imaging; YOLO instance segmentation; anatomical regions; sea-caught versus farmed; non-destructive detection

Key Contribution: This study presents an internally fish-validated workflow that combines YOLO11n-seg with anatomical-region hyperspectral extraction and sea-caught versus farmed collection-source discrimination. Region-specific analysis enables spectral characteristics of different anatomical regions to be examined separately. This study does not establish superiority over whole-fish analysis, externally validated provenance authentication, or causal effects of collection source.

Check for updates

Academic Editor: Zhangying Ye

Received: 17 July 2026
Revised: 15 August 2026
Accepted: 17 August 2026
Published: 19 August 2026

Copyright: © 2026 by the authors. Licensee MDPI, Basel, Switzerland. This article is an open access article distributed under the terms and conditions of the Creative Commons Attribution (CC BY) license.

1. Introduction

Large yellow croaker (*Larimichthys crocea*) is one of the most economically important marine aquaculture species in China owing to its high market value and strong consumer demand [1]. The expansion of artificial breeding and cage culture has increased farmed production. Previous work has reported group-level morphological and quality differences between sea-caught and farmed fish [2,3], and mislabeling remains a market concern. However, the labels used in observational studies may represent collection channels rather than independently verified provenance. A rapid, non-destructive, and interpretable method for sea-caught versus farmed collection-source discrimination could therefore support exploratory quality assessment, provided that conclusions remain within the verified scope of the sampling and validation design.

Differences between sampled fish groups may be associated with morphology, body surface pigmentation, nutritional composition, tissue texture, and collection or handling conditions [4]. These source-associated patterns may vary among anatomical regions. Yao et al. [5] reported morphological differences between sea-caught and farmed large yellow croaker using conventional images and artificial intelligence methods. On this basis, the head, eye, dorsal region, abdominal region, pectoral fin, and caudal fin were treated as predefined analytical regions. Region-specific analysis enables the spectral characteristics of these anatomical regions to be examined separately; no matched whole-fish baseline was available to test comparative superiority.

With the rapid development of computer vision [6] and deep learning [7], tasks such as individual fish recognition, object detection [8], contour segmentation, and category assessment have gradually become automated [9]. In aquaculture scenarios, non-contact image-based sensing [10] can reduce manual intervention and provide a data basis for aquaculture environment monitoring, phenotypic measurement and evaluation [11], and sustainable aquaculture management [12,13]. For the large yellow croaker industry, disease risk, quality fluctuation, and product mixing remain practical challenges. Therefore, the development of scalable and automated visual inspection [12] and trait-analysis methods is urgently needed [14]. In visual phenotyping studies, whole-fish segmentation, detection, and subsequent morphological measurement represent common analytical pipelines. Many studies have focused on tasks such as individual contour segmentation, species recognition, and size estimation. For example, the DeepFish dataset [15], developed for market-tray scenarios, provides instance segmentation annotations together with species and size information, thereby offering an important benchmark for evaluating instance segmentation methods. Zhang et al. [16] combined YOLOv5 with principal component analysis to perform carapace object detection and recognition in Chinese mitten crab, further demonstrating the potential of deep learning-based visual analysis in aquatic phenotyping. In underwater or turbid-water environments, however, image blur, geometric distortion, and low contrast can substantially reduce segmentation accuracy. To address these visibility-related challenges, researchers have proposed improved network architectures for underwater fish segmentation [17]. Wang et al. [18] used a laser imaging method to measure the posture and body size of fusiform fish. These studies indicate that different anatomical regions and morphological structures of fish contain important phenotypic information.

However, anatomical-region-level analysis [19] is not equivalent to whole-fish segmentation in terms of task characteristics. Body regions, particularly fins and eyes, are often smaller and more elongated, and they are more likely to be missed under dense schooling conditions or mutual occlusion. Meanwhile, anatomical-region-level annotation may involve ambiguities in boundary delineation or anatomical definition, such as changes in the extension angle of the pectoral fin and morphological variation caused by caudal

fin movement. In response to pixel-level annotation and analysis tasks at the anatomical-region level, public resources and methods that are more closely aligned with biological interpretation have begun to emerge. For example, researchers proposed Fish-Vista, a dataset for fish visual trait analysis, including trait segmentation tasks, emphasizing the analysis of visible traits from local anatomical regions [20]. Yao et al. [21] applied YOLOv11-CBAM to morphological measurement of large yellow croaker based on X-ray images, achieving automatic segmentation of structures such as the fish body, swim bladder, spine, eye, and otolith.

Hyperspectral imaging integrates image and spectral information and can capture continuous wavelength-dependent responses under non-contact conditions. In this study, the measurements were expressed as relative reflectance ratios because only an in-scene white reference was available. The method was used to examine source-associated spectral differences between sea-caught and farmed collection groups, rather than to infer causal biological mechanisms or verified geographic provenance. The overall technical workflow is illustrated in Figure 1.

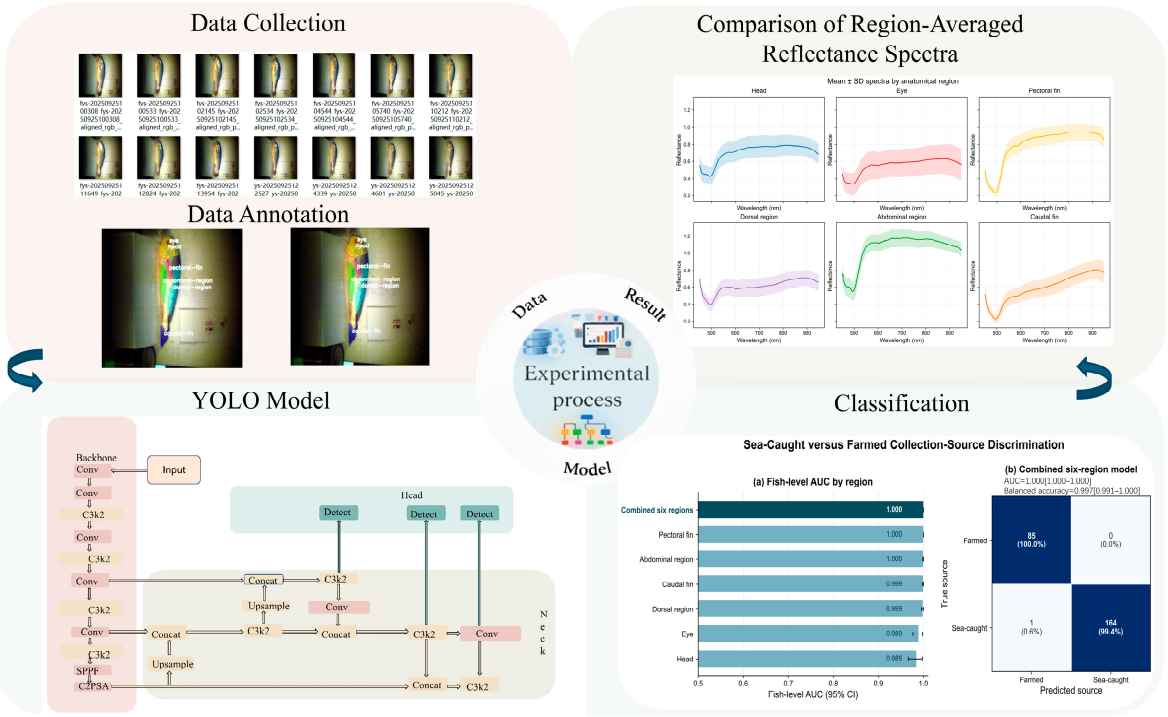


Figure 1. Technical workflow for preliminary sea-caught versus farmed collection-source discrimination using hyperspectral features extracted from six anatomical regions. Different colors indicate the segmented anatomical regions of the large yellow croaker, including the eye, head, pectoral fin, abdominal region, dorsal region, and caudal fin.

This study evaluated whether hyperspectral features from six anatomical regions could discriminate between the sea-caught and farmed collection-source labels represented in the available cohort. The workflow comprised fish-level dataset construction, YOLO11n-seg instance segmentation, relative white-reference normalization, wavelength-wise statistical analysis, PCA visualization, and internal fish-grouped source classification. The objective was to quantify internal predictive performance and source-associated spectral patterns while explicitly accounting for unverified provenance, incompletely recorded confounders, relative calibration, the absence of a matched whole-fish baseline, and the absence of an independent external cohort.

2. Materials and Methods

2.1. Sample Collection

Farmed large yellow croaker were obtained through cage-culture collection channels in the East China Sea, whereas the sea-caught group was assigned from the original capture collection channel in the East China Sea. These were operational collection-source labels. The archived materials did not retain complete per-fish capture coordinates, farm or cage identifiers, feed history, vessel records, collection dates, age, sex, season, geographic origin, body condition, capture conditions, storage duration, surface moisture, or acquisition-batch records. No independent genetic, chemical, documentary, nor traceability verification was performed. Provenance records that were not retained were not reconstructed. Consequently, the analyses address source-associated differences between the two collection groups and do not establish verified provenance or causal effects of collection source. The sample composition is summarized in Table 1.

Table 1. Sea-caught and farmed large yellow croaker included in the hyperspectral analysis.

Collection-Source Group	Samples (*n*)	Percentage	Available Anatomical Regions	Recorded Acquisition Controls and Limitations
Sea-caught group	171	66.3%	Head, eye, pectoral fin, caudal fin, dorsal region, and abdominal region	Fish of similar body length were selected whenever possible. Freezing temperature, freezing duration, and thawing conditions were kept as consistent as possible.
Farmed group	87	33.7%	Head, eye, pectoral fin, caudal fin, dorsal region, and abdominal region	Fish of similar body length were selected whenever possible. Freezing temperature, freezing duration, and thawing conditions were kept as consistent as possible.
Total	258	100.0%	Six anatomical regions	Body-size selection and freezing conditions were kept as consistent as possible between the two groups.

2.2. Experimental Equipment and Illumination Conditions

In this study, a handheld hyperspectral imaging system (ATH2000, OPTOSKY, Xiamen, China) was used to acquire hyperspectral image data from large yellow croaker samples. The experimental setup mainly consisted of a hyperspectral camera, a standard white reference board, supplementary illumination sources, and a data acquisition control terminal. The hyperspectral camera covered the visible to near-infrared spectral range of 400–1000 nm, with high spectral and spatial resolution, making it suitable for non-contact measurement of surface spectral information.

2.2.1. Hyperspectral Camera

Figure 2 presents the OPTOSKY ATH2000 handheld visible–near-infrared hyperspectral imaging system used in this study (Xiamen, China). The instrument operates over a wavelength range of 400–1000 nm. The system integrates an imaging lens and a hyperspectral imaging camera and is equipped with a 1920 × 1200-pixel CCD sensor. It provides high spatial and spectral resolution, with an optimal spectral resolution of up to 1.5 nm, as well as good imaging linearity and low noise levels. Therefore, it is suitable for high-precision acquisition of spectral information from various objects and application scenarios.



Figure 2. ATH2000 handheld visible–near-infrared hyperspectral imaging system. The system operates over the 400–1000 nm spectral range and was used for hyperspectral image acquisition of large yellow croaker samples.

The ATH2000 uses a built-in scanning mechanism to acquire the second spatial dimension while recording the spatial–spectral line data. Therefore, the three-dimensional hyperspectral data cube was generated by the internal scanner, and manual translation or rotation of the camera was not required during acquisition. The fish and white reference board remained stationary during each scan.

The device has a compact handheld design, an Android interface, a touchscreen, and onboard storage. These features facilitated acquisition and data review under the controlled setup used in this study; field performance was not evaluated independently.

2.2.2. Illumination Conditions

To ensure illumination stability and spectral uniformity during hyperspectral image acquisition, OSRAM halogen lamps provided by Jingyi Optoelectronics Co., Ltd. (Guangzhou, China), were used as supplementary light sources. The lamps emitted a continuous spectrum covering approximately 350–2500 nm, with a smooth radiative energy distribution. In particular, they exhibited high spectral stability from the visible to near-infrared regions, thereby satisfying the requirements of hyperspectral reflectance imaging for continuous and uniform illumination.

Figure 3 illustrates the illumination arrangement. The halogen lamps were positioned on both sides of the camera at approximately 45° relative to the sample surface and about 30 cm from the samples. The lamps were preheated for 5–10 min, and other ambient light sources were turned off during imaging. Lamp positions and acquisition settings were held constant within the reported protocol. These controls supported within-protocol comparability, but repeatability across lamp positions, exposure settings, sessions, or devices was not evaluated.

2.3. Annotation of Anatomical Regions and Dataset Construction

The analytical hyperspectral dataset contained 258 fish, including 171 sea-caught and 87 farmed individuals, yielding 1533 usable fish-by-region spectra across six anatomical regions, with slight variation in sample availability among regions. The archive contained 289 RGB preview images corresponding to the hyperspectral acquisitions; these images were not considered independent biological replicates. Of these, 101 annotated images were linked by filename-based sample IDs to 101 unique fish in the spectral dataset and were partitioned into 71 training images (36 sea-caught and 35 farmed), 20 validation images (10 sea-caught and 10 farmed), and 10 test images (5 sea-caught and 5 farmed). Each annotated image corresponded to a unique fish, and no sample IDs overlapped among the three splits.

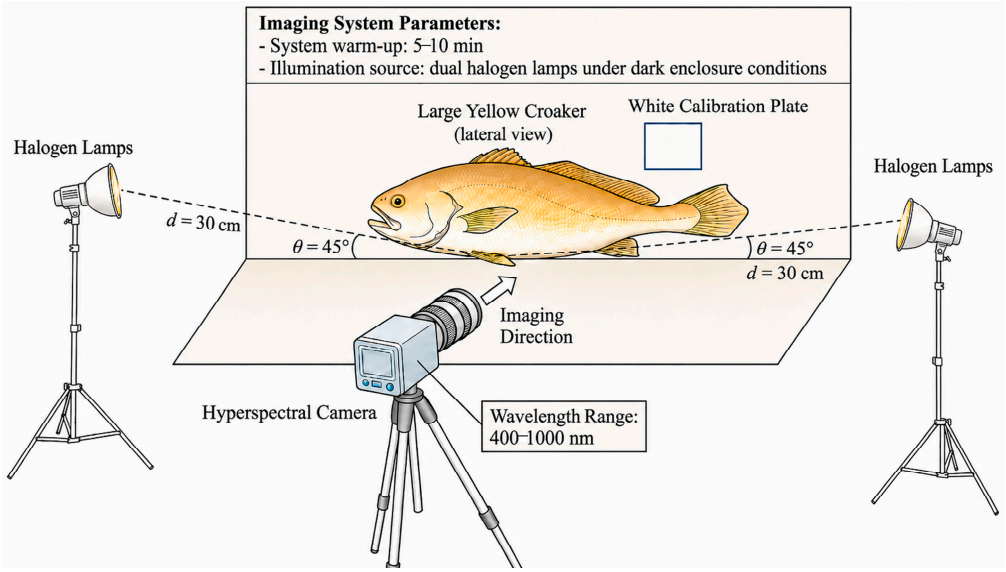


Figure 3. Schematic diagram of the hyperspectral imaging system and dual halogen lamp illumination arrangement for large yellow croaker.

During annotation, instance-level polygon annotation was performed for the key anatomical regions of large yellow croaker according to local anatomical structures and the requirements of spectral extraction. The annotated categories included the head, eye, dorsal region, abdominal region, pectoral fin, caudal fin, and white reference board. Specifically, the head region mainly covered the main head tissue from the snout to the vicinity of the operculum. The eye region was annotated according to the visible outline of the fish eye. The dorsal region was located along the upper dorsal line of the fish body and covered the dorsal muscle and the area with relatively distinct body surface coloration. The abdominal region was located along the lower ventral line of the fish body and covered the abdominal muscle and the body surface reflection area. The pectoral fin region was annotated according to the visible boundary of the pectoral fin. The caudal fin region covered the fin rays and the visible outline of the tail fin. The white reference board was annotated as the effective reflective area of the standard white board in the image, which was used for subsequent white-reference normalization and relative white-reference normalization. For image regions affected by shadows, strong specular reflection, blurred edges, or unclear tissue boundaries, the annotation boundary was determined based on clearly identifiable fish structures, while background areas, the edges of the white reference board, and non-target regions were excluded from the target mask as much as possible.

Consistent anatomical-region definitions were maintained across samples during annotation. Polygon annotations delineated the head, eye, dorsal region, abdominal region, pectoral fin, caudal fin, and white reference board. All annotations were checked image by image for overlaps, boundary extension, reference-board coverage, and missed small targets. The resulting masks were mapped to the relative white-reference normalization hyperspectral cubes to extract regional mean relative reflectance ratios. An example annotation is shown in Figure 4.

2.4. Construction of the YOLO-Based Instance Segmentation Model for Anatomical Regions

The implemented model was the standard Ultralytics YOLO11n-seg instance segmentation model (Ultralytics version 8.3.124) initialized from yolo11n-seg.pt pretrained weights. No custom architectural blocks were introduced. Model selection used the 20-image validation split. Aggregate metrics reported from the training record therefore correspond

to this validation split; the 10-image test split was evaluated separately for final per-class reporting in Table 2 and was not treated as an independent external cohort.

Table 2. Per-class YOLO11n-seg mask performance on the separate 10-image test split (5 sea-caught and 5 farmed; 70 annotated instances).

Class	Mask Precision	Mask Recall	Mask mAP@0.5	Mask mAP@0.5–0.95
Head	0.942	1.000	0.995	0.828
Eye	1.000	0.965	0.995	0.495
Pectoral fin	1.000	0.977	0.995	0.573
Dorsal region	0.944	1.000	0.995	0.642
Abdominal region	0.952	1.000	0.995	0.442
Caudal fin	0.946	1.000	0.995	0.734
White reference board	0.942	1.000	0.995	0.947

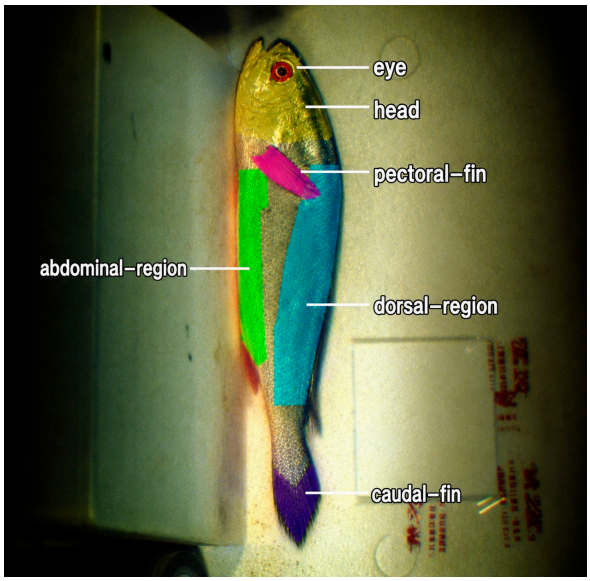


Figure 4. Example YOLO11n-seg instance annotation for large yellow croaker. Polygon masks delineate head, eye, pectoral fin, dorsal region, abdominal region, caudal fin, and in-scene white reference board.

Training used 640 × 640-pixel inputs, a batch size of 4, at most 300 epochs, an early-stopping patience of 100, automatic optimizer selection, an initial learning rate of 0.01, a final learning-rate fraction of 0.01, a momentum of 0.937, a weight decay of 0.0005, a random seed of 0, deterministic execution, and automatic mixed precision. Augmentation comprised Mosaic (probability: 1.0; disabled during the final 10 epochs), horizontal flipping (0.5), translation (0.10), scaling (0.50), and HSV perturbation (hue: 0.015; saturation: 0.70; value: 0.40). Vertical flipping, rotation, MixUp, CutMix, and Copy–Paste were not used. Evaluation used the Ultralytics default confidence threshold for metric integration and an intersection-over-union threshold of 0.70 for non-maximum suppression. Training and evaluation were performed with PyTorch 2.8.0 and CUDA 12.8 on an NVIDIA RTX A5000 GPU with 24 GB of memory.

The YOLO series models have been widely applied in real-time object detection tasks because of their single-stage architecture, end-to-end training paradigm, and fast inference speed. Early versions, including YOLOv1–YOLOv3, formulated object detection as a joint regression problem involving bounding-box localization and class probability prediction, thereby establishing the basic paradigm of one-stage detection models. Subsequently, the YOLO series has been continuously optimized in terms of feature extraction networks,

multi-scale feature fusion, loss function design, and training strategies and has gradually been extended to more complex real-time visual tasks [22–25]. In recent years, with the increasing demand for instance segmentation in industrial inspection, agricultural vision, and biological phenotyping, YOLO-based models have been further extended from object detection to instance segmentation. Represented by the Ultralytics YOLO segmentation models, these methods predict instance mask-related parameters in addition to bounding boxes and class information and generate target instance masks through the combination of prototype masks and mask coefficients [26]. This strategy of "prototype mask generation + instance coefficient prediction" is consistent with the real-time instance segmentation framework proposed in YOLACT, in which a set of shared prototype masks is first generated and then linearly combined using instance-specific coefficients to obtain target masks while maintaining high segmentation efficiency [27]. Therefore, YOLO-based instance segmentation models combine fast detection capability with mask generation ability, making them suitable for rapid, batch-wise, and standardized extraction of local anatomical regions.

Compared with two-stage instance segmentation methods, YOLO-based instance segmentation models are more suitable for the scenario of this study. Mask R-CNN, as a representative two-stage instance segmentation method, obtains high-quality instance masks through region proposal generation, ROI alignment, and a mask branch. However, its multi-stage architecture usually leads to higher computational complexity and greater inference latency [28]. Mask2Former, which follows the Transformer-based segmentation framework, uses masked attention to process semantic segmentation, instance segmentation, and panoptic segmentation within a unified framework and shows strong segmentation performance. Nevertheless, its training and deployment are relatively complex and require greater computational resources and larger-scale datasets [29]. In addition, box-free instance segmentation methods such as SOLO and SOLOv2 generate instance masks through location grouping or dynamic convolution kernels, reducing dependence on detection boxes and balancing speed and accuracy [30]. However, the primary objective of this study was not to pursue the upper limit of general instance segmentation performance in complex scenes but to stably obtain segmentation masks of different anatomical regions of large yellow croaker under limited annotated samples and apply them to regional spectral extraction from hyperspectral images. Therefore, the YOLO instance segmentation model, which is relatively lightweight in structure, mature in training workflow, efficient in inference, and easy to deploy, better meets the application requirements of this study. The overall architecture of the YOLO instance segmentation model adopted in this study is presented in Figure 5.

YOLO11n-seg was used to segment six predefined anatomical regions and the in-scene white reference board from RGB previews aligned with the hyperspectral data. The resulting masks were mapped to the corresponding hyperspectral cubes to extract mean relative reflectance ratios for each anatomical region. Region-specific analysis enables the spectral characteristics of different anatomical regions to be examined separately. Because a compatible matched whole-fish mask and mean spectrum were not retained for every fish, this workflow was not compared with a whole-fish baseline, and no claim of regional superiority is made.

2.5. Relative White-Reference Normalization

Relative white-reference normalization was applied to reduce within-scene multiplicative illumination variation. The fish and a Spectralon white reference board were imaged in the same scene, and each target digital response was divided by the wavelength-specific mean response of the reference ROI. No dark-reference images were acquired. Accordingly,

the resulting measurements are reported as relative reflectance ratios, not absolute or fully radiometrically calibrated reflectance.

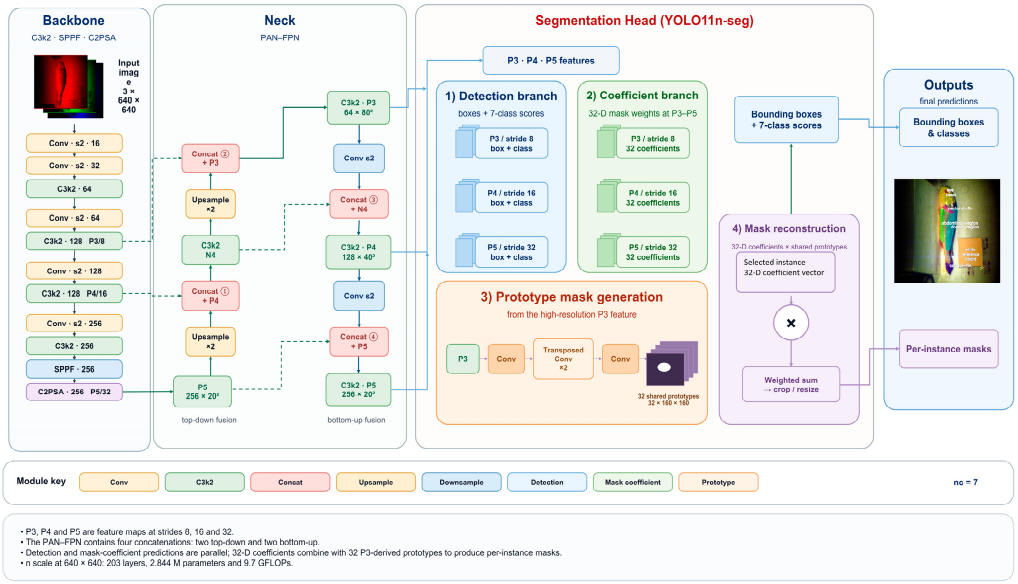


Figure 5. Schematic architecture of the implemented standard YOLO11n-seg instance segmentation model.

During image acquisition, a standard Spectralon white reference board was placed within the same field of view as the target, so that it presented the same illumination conditions and geometric configuration as the sample to be measured. To avoid interference caused by specular reflection, the white reference board and the sample surface were positioned approximately perpendicular to the optical axis of the camera, with an angle of approximately 45° between the incident light and the observation direction. The hyperspectral image cube was acquired under fixed exposure time and gain settings, ensuring that the target region and the white reference region appeared simultaneously in the same image frame. This arrangement ensured that both regions were imaged under the same incident irradiance, thereby maintaining illumination consistency.

During processing, the mean digital response of the white-reference ROI was calculated at each wavelength. For a target pixel p at wavelength λ, the working relative reflectance ratio was calculated as Rrel(p, λ) = DNtarget(p, λ)/DNwhite(λ).

Here, DNtarget(p, λ) is the target-pixel digital response, and DNwhite(λ) is the mean white-reference digital response measured in the same image. Because dark-reference images were not acquired, dark current and other additive detector effects were not subtracted. The ratio may reduce within-scene multiplicative illumination variation, but it is not equivalent to standard white-and-dark radiometric calibration.

$$R_{\mathrm{rel}}(p,\lambda) = \frac{DN_{\mathrm{target}}(p,\lambda)}{DN_{\mathrm{white}}(\lambda)} \quad (1)$$

The same-scene ratio was used consistently throughout the analysis. Its interpretation is restricted to relative comparisons within the present acquisition protocol.

Repeatability was not evaluated across repeated scans, lamp positions, exposure settings, acquisition sessions, or devices. The analysis therefore does not establish absolute reflectance accuracy, complete radiometric correction, or cross-session calibration reliability.

The white-reference ROI occupied more than approximately 3% of image pixels and was positioned away from image edges. These controls supported internal comparabil-

ity only; the absence of dark-reference images and repeatability experiments remains a limitation. The reference ROI and its annotation are shown in Figure 6.



(**a**) (**b**)

Figure 6. White-reference ROI used for in-scene relative white-reference normalization. (**a**) Pseudo-color hyperspectral image containing the fish and Spectralon reference board; (**b**) annotated reference ROI used as the wavelength-specific denominator. No dark-reference image was acquired, so dark current and additive detector effects were not subtracted.

2.6. Relative Reflectance-Ratio Data Processing and Spectral Feature Analysis

2.6.1. Organization of Hyperspectral Mean Spectral Data

After anatomical-region masks were applied, the wavelength-specific target responses were divided by the in-scene white-reference response to obtain mean relative reflectance ratios. The resulting wide-format table contained one row per fish and anatomical region, together with sample ID, collection-source label, anatomical-region label, and wavelength-specific relative reflectance ratios.

Let $\Omega_{i,m}$ denote the mask region of the m-th anatomical region in the i-th sample, and let $N_{i,m}$ denote the number of valid pixels contained in this region. The mean relative reflectance ratio of this region in the k-th band can then be expressed as:

$$x_{i,m,k} = \frac{1}{N_{i,m}} \sum_{(u,v)\in\Omega_{i,m}} R_i(u, v, \lambda_k) \tag{2}$$

For each fish and anatomical region, the regional mean relative reflectance ratio at a wavelength was calculated by averaging the pixel-level relative ratios within the corresponding mask.

Furthermore, the mean spectral vector of the m-th anatomical region in the i-th sample can be expressed as:

$$\mathrm{x}_{i,m} = [x_{i,m,1}, x_{i,m,2}, \ldots, x_{i,m,K}] \tag{3}$$

The mean regional spectral vector comprised the relative reflectance ratios across the retained wavelengths. Collection-source labels were read from the archived sample identifier and classified as farmed or sea-caught.

Region-specific analysis enabled spectral characteristics of the six anatomical regions to be examined separately. A compatible whole-fish mask and whole-fish mean spectrum were not retained for every fish. This study therefore did not test whether regional models outperformed a matched whole-fish baseline.

2.6.2. Selection of Effective Spectral Bands

The original wavelength range of the hyperspectral data was approximately 397.15–1005.85 nm. Considering that hyperspectral sensors usually show unstable responses, relatively low signal-to-noise ratios, and large spectral fluctuations at both ends of the spectral range, band selection was performed before subsequent analysis. Only the effective bands within the range of 450–950 nm were retained for spectral curve plotting, difference analysis, principal component analysis, and classification modeling. This

wavelength range lies within the visible-to-near-infrared region and can preserve the main spectral information related to fish body surface color, pigment absorption, tissue scattering, and water content while reducing the influence of noise from the short- and long-wavelength ends on result interpretation.

The selected effective band set was defined as follows:

$$\Lambda' = \{\lambda_t \mid 450 \leq \lambda_t \leq 950, t = 1, 2, \ldots, T\} \tag{4}$$

where Λ' denotes the set of effective bands retained after band selection, λ_t denotes the central wavelength corresponding to the t-th effective band after selection, and T denotes the number of effective bands retained within the range of 450–950 nm.

On this basis, the selected mean spectral vector of the m-th anatomical region in the i-th sample can be expressed as:

$$\mathbf{x}'_{i,m} = \left[x'_{i,m,1}, x'_{i,m,2}, \ldots, x'_{i,m,T}\right], \lambda_t \in \Lambda' \tag{5}$$

where $\mathbf{x}'_{i,m}$ denotes the effective mean spectral vector of the m-th anatomical region in the i-th sample after band selection, $x'_{i,m,t}$ denotes the mean relative reflectance ratio of this region in this sample at the t-th selected effective band, i is the sample index; m is the anatomical-region index, and $t = 1, 2, \ldots, T$ is the index of the selected effective band. All subsequent spectral statistical analyses, graphical visualization, principal component analysis, and classification modeling were performed based on the selected effective bands.

2.6.3. Calculation and Visualization of Mean Spectra for Different Anatomical Regions

To compare spectral differences among different anatomical regions, the selected mean spectra were grouped according to anatomical-region categories. The mean relative reflectance-ratio values of the head, eye, pectoral fin, dorsal region, abdominal region, and caudal fin were calculated at each effective wavelength. For the m-th anatomical region, its mean relative reflectance ratio at wavelength λ_t can be expressed as:

$$\overline{R}_m(\lambda_t) = \frac{1}{N_m} \sum_{i=1}^{N_m} x'_{i,m,t} \tag{6}$$

In this equation, $\overline{R}_m(\lambda_t)$ denotes the mean relative reflectance ratio of the m-th anatomical region at wavelength λ_t. N_m represents the number of valid spectral samples corresponding to this region. The term $x'_{i,m,t}$ refers to the selected mean relative reflectance ratio of the i-th sample in the m-th anatomical region at wavelength λ_t. Here i is the sample index, and m is the anatomical-region index. The variable $t = 1, 2, \ldots, T$ denotes the index of the selected effective bands, with T representing the total number of effective bands retained after band selection.

Moreover, the standard deviation at each wavelength was calculated for each anatomical region to characterize inter-sample variability. The spectra were visualized as mean curves with standard deviation shading. This representation provides an intuitive overview of regional differences in relative reflectance-ratio magnitude, spectral shape, and variability, thereby supporting the subsequent identification of key anatomical regions and potentially informative wavelengths.

2.6.4. Region-Specific Spectral Difference Analysis Between Sea-Caught and Farmed Samples

Source-associated spectral differences were examined by grouping fish according to collection source and anatomical region. For each anatomical region, the farmed and sea-caught mean relative reflectance ratios were calculated separately at each wavelength.

$$\overline{R}_m^F(\lambda_t) = \frac{1}{N_m^F}\sum_{i=1}^{N_m^F} x_{i,m,t}^{F\prime},\ \overline{R}_m^W(\lambda_t) = \frac{1}{N_m^W}\sum_{i=1}^{N_m^W} x_{i,m,t}^{W\prime} \tag{7}$$

The wavelength-wise mean contrast was defined as farmed minus sea-caught. This descriptive contrast indicates the direction of the observed source association but does not identify a causal mechanism.

$$\Delta R_m(\lambda_t) = \overline{R}_m^F(\lambda_t) - \overline{R}_m^W(\lambda_t) \tag{8}$$

A positive contrast indicates a higher mean relative reflectance ratio in the farmed group, whereas a negative contrast indicates a higher mean relative reflectance ratio in the sea-caught group.

2.6.5. Fish-Level Effect Sizes, Confidence Intervals, and Multiple-Comparison Control

For each anatomical region and wavelength, the farmed-minus-sea-caught standardized mean difference was quantified using Cohen's d. Uncertainty was estimated by 2000 stratified bootstrap resamples at the fish level, sampling the two collection-source groups separately. Two-sided Welch's *t*-tests were performed at each wavelength, and Benjamini–Hochberg false-discovery-rate correction was applied separately within each anatomical region across the 246 tested wavelengths. Bands with adjusted *p*-values (q) < 0.05 were considered statistically supported. Fish, rather than images or pixels, were the independent units.

$$d_m(\lambda_t) = \frac{\overline{R}_m^F(\lambda_t) - \overline{R}_m^W(\lambda_t)}{s_{p,m}(\lambda_t)} \tag{9}$$

In the effect-size equation, d denotes the standardized farmed-minus-sea-caught contrast for an anatomical region and wavelength. Positive values indicate higher relative reflectance ratios in farmed fish; negative values indicate higher values in sea-caught fish.

$$s_{p,m}(\lambda_t) = \sqrt{\frac{(N_m^F-1)\left[s_m^F(\lambda_t)\right]^2 + (N_m^W-1)\left[s_m^W(\lambda_t)\right]^2}{N_m^F+N_m^W-2}} \tag{10}$$

The group sample sizes varied slightly among anatomical regions because of missing masks or spectra. Consequently, the exact sea-caught and farmed fish counts are reported with the results. Effect sizes were interpreted as descriptive wavelength-wise contrasts and were not used alone to rank predictive performance.

2.6.6. Principal Component Analysis

To visualize the distribution of different anatomical regions and samples in the overall spectral feature space, principal component analysis (PCA) was applied to reduce the dimensionality of the high-dimensional spectral data. Considering that overall relative reflectance-ratio magnitude may vary among samples, each spectrum was first processed using standard normal variate (SNV) transformation before PCA. This preprocessing step was used to reduce the influence of baseline shifts and overall intensity differences on the distribution of principal components. For the *i*-th spectrum, let $x_{i,t}$ denote its relative reflectance ratio at the *t*-th effective band. The mean and standard deviation of this spectrum across all effective bands were calculated as follows:

$$\overline{x}_i = \frac{1}{T}\sum_{t=1}^{T} x_{i,t} \tag{11}$$

$$s_i = \sqrt{\frac{1}{T-1}\sum_{t=1}^{T}(x_{i,t} - \overline{x}_i)^2} \quad (12)$$

On this basis, the spectral variable after SNV preprocessing was defined as:

$$z_{i,t} = \frac{x_{i,t} - \overline{x}_i}{s_i} \quad (13)$$

In this equation, $x_{i,t}$ represents the relative reflectance ratio of the i-th spectrum at the t-th effective band. The term refers to the mean relative reflectance ratio $\overline{x}_i$ of the i-th spectrum across all effective bands, while s_i is the corresponding standard deviation. After SNV preprocessing, the standardized spectral value of the i-th spectrum at the t-th effective band is given by $z_{i,t}$. Here T indicates the number of effective bands retained after band selection. After SNV preprocessing, PCA was performed to extract the first two principal components for two-dimensional scatter plot visualization. The basic principle of PCA is to project the original high-dimensional spectral variables onto a new set of mutually orthogonal variables, so that the first few principal components retain as much of the major variation in the original data as possible. By coloring the PCA scatter plots according to anatomical region and source category, the spectral structural differences among different anatomical regions, as well as the distribution patterns of sea-caught and farmed samples in the principal component space, could be visually examined.

2.6.7. Sea-Caught Versus Farmed Collection-Source Classification and Internal Fish-Level Validation

Binary collection-source models were fitted separately for each of the six anatomical regions and for a combined six-region dataset. The combined dataset included only fish with all six anatomical regions, with the six regional spectra concatenated into one fish-level feature vector. Sea-caught fish were the positive class.

Five-fold StratifiedGroupKFold cross-validation was used as internal fish-level validation, with fish identity as the grouping variable and collection source as the stratification variable. All observations from the same fish were assigned exclusively to either the training or validation portion of a fold. The wavelength interval was fixed a priori at 450–950 nm. In the logistic-regression pipeline, feature standardization was fitted only on each training fold and then applied to its held-out fold. No outcome-guided wavelength selection was performed before cross-validation. Out-of-fold probabilities were reduced to one prediction per fish before evaluation, preventing fish-level leakage. No independent external validation cohort from different farms, capture locations, seasons, or collection periods was available.

Two classifiers were evaluated: logistic regression and random forest. Model hyperparameters were fixed without data-driven tuning: logistic regression used the liblinear solver, balanced class weights, and 3000 maximum iterations, whereas random forest used 400 trees, balanced-subsample class weights, and a minimum leaf size of two. Accuracy, sensitivity, specificity, balanced accuracy, F1-score, ROC curves, and AUC were calculated from fish-level out-of-fold predictions; further, 95% confidence intervals used 2000 stratified fish-level bootstrap resamples. As a sensitivity analysis for the combined six-region logistic-regression model, 10 repeated five-fold fish-grouped cross-validations were performed with different split seeds while keeping standardization within each training fold. A 200-permutation fish-level label test used the same grouped folds and compared the observed AUC with the permuted-label null distribution. These analyses assess internal robustness only and do not constitute external validation.

3. Results

3.1. Dataset Characteristics and Anatomical-Region Segmentation Performance

The cohort comprised 258 unique fish (171 sea-caught and 87 farmed) and 1533 usable fish-by-region spectra. The 101-image segmentation subset was linked to 101 unique fish and split into 71 training, 20 validation, and 10 test images, with no linked fish-ID overlap. Figure 7 summarizes sample flow, class balance, regional availability, exclusions from the combined model, and the segmentation split.

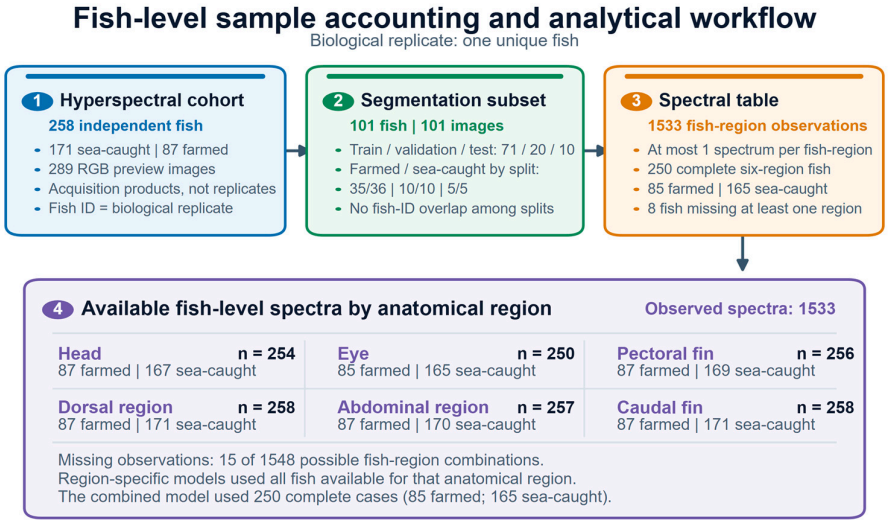


Figure 7. Fish-level sample accounting and analytical workflow.

The training and validation curves in Figure 8 show early loss reduction followed by stabilization. On the 20-image validation set (10 sea-caught and 10 farmed; 140 annotated instances), bounding-box precision was 0.976, recall was 0.983, mAP@0.5 was 0.981, and mAP@0.5–0.95 was 0.700. The corresponding mask precision, recall, mAP@0.5, and mAP@0.5–0.95 were 0.969, 0.976, 0.972, and 0.669, respectively. Thus, these aggregate YOLO metrics correspond to the validation split, not the separate 10-image test split. Table 2 reports per-class metrics calculated separately on the 10-image test split (5 sea-caught and 5 farmed; 70 annotated instances). This test split was held out from model selection but was drawn from the same source dataset and is not an independent external cohort.

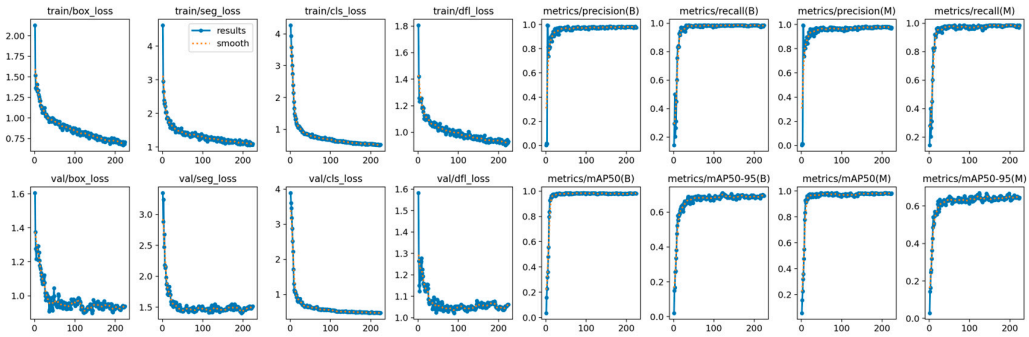


Figure 8. YOLO11n-seg training and validation curves. The aggregate bounding-box and mask precision, recall, mAP@0.5, and mAP@0.5–0.95 shown by these curves were calculated on the 20-image validation set (10 sea-caught and 10 farmed; 140 annotated instances), not on the separate 10-image test split.

The per-class test metrics in Table 2 were generated from the archived best.pt model and test split; the validation-set aggregate metrics were read from the saved training results at the selected best-model epoch. The two sets of values are therefore not interchangeable.

Each test image was linked to one unique fish and contained one annotated instance of each of the seven classes. Test-split values are reported separately and were not substituted for the 20-image validation-set aggregate metrics.

3.2. Mean Spectral Characteristics of Different Anatomical Regions

After relative white-reference normalization, effective-band selection, and regional spectral extraction, mean relative reflectance-ratio spectra were obtained for head, eye, pectoral fin, dorsal region, abdominal region, and caudal fin over 450–950 nm. As shown in Figure 9, the spectra differ among anatomical regions. These descriptive patterns are compatible with region-dependent optical responses but do not identify their biological causes.

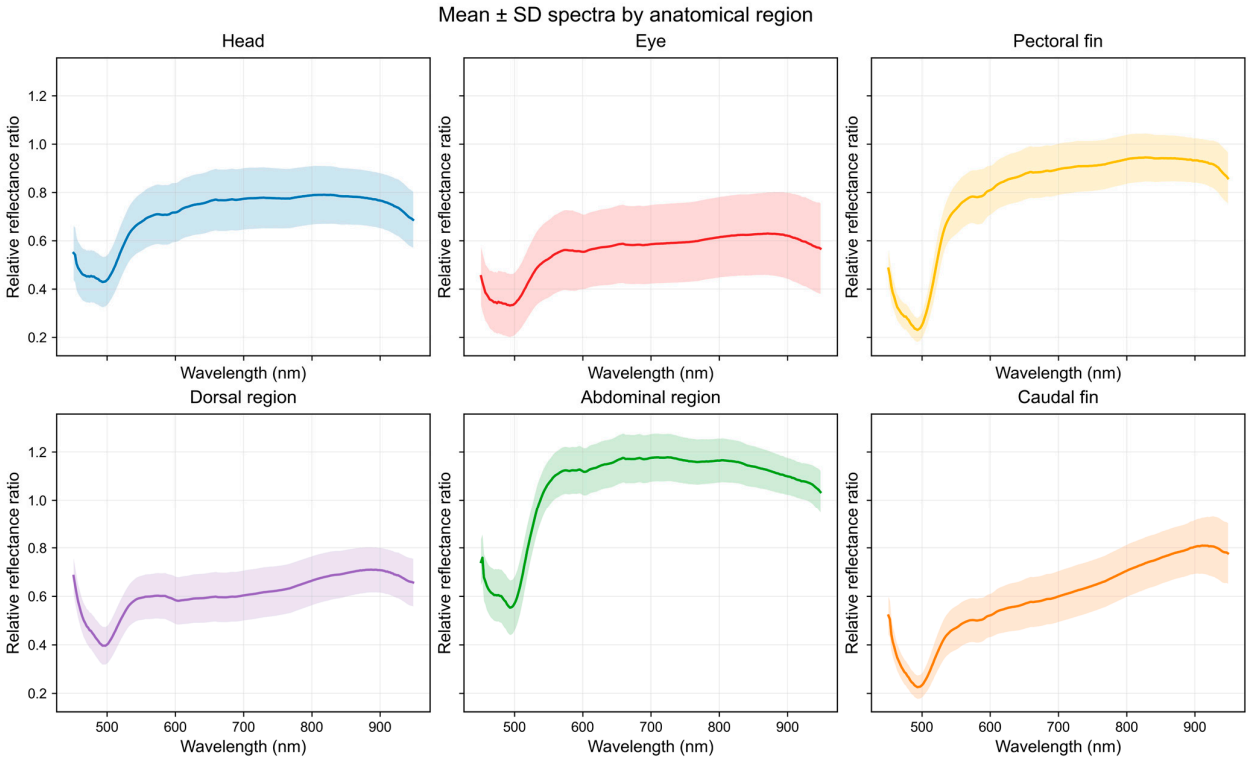


Figure 9. Region-averaged relative reflectance-ratio spectra (mean ± SD) for the head, eye, pectoral fin, dorsal region, abdominal region, and caudal fin over 450–950 nm. All panels use a common vertical scale.

Overall, all anatomical regions show a clear decrease in the relative reflectance ratio around 480–500 nm, followed by a rapid increase after 520 nm. As the wavelength extends into the long-wavelength visible and near-infrared regions, the curves gradually becomes stable or continues to increase. This common trend suggests that the body surface of large yellow croaker exhibits strong absorption features in the blue–green region while showing higher relative reflectance ratios in the red to near-infrared regions.

Differences in relative reflectance-ratio magnitude among anatomical regions are also evident. The abdominal region shows the highest overall relative reflectance ratios and maintains a relatively high level within 600–850 nm. The pectoral fin also exhibits relatively high relative reflectance ratios, which gradually stabilize after 650 nm. The head and the dorsal region show moderate relative reflectance-ratio levels. By contrast, the eye has the lowest overall relative reflectance ratios, particularly in the visible region, indicating strong absorption. The caudal fin shows relatively low relative reflectance ratios in the short-wavelength region, but its relative reflectance ratio continues to increase

with wavelength and gradually approaches those of the dorsal region and the head in the near-infrared region.

The spectral curve of the abdominal region is clearly higher than those of the other regions across most wavelengths. This may be related to its lighter body surface color, tissue thickness, and local scattering properties. Although both the pectoral fin and caudal fin are fin structures, their spectral patterns are not completely consistent. The pectoral fin's spectral pattern increases rapidly after 550 nm and forms a relatively high plateau in the near-infrared region. The caudal fin's spectral pattern, however, shows a more continuous upward trend, suggesting that different fin regions still differ in tissue structure, thickness, and light transmittance. The eye curve remains relatively low overall and shows a wider standard deviation range, indicating that the eye region may be more strongly affected by pigmentation, curved-surface reflection, and segmentation errors of small targets. Its spectral stability is therefore weaker than that of larger regions such as the abdominal region and the pectoral fin.

3.3. Within-Group Variability and Source-Specific Spectra

Figure 10 compares the farmed and sea-caught group means and standard deviations for each anatomical region. The bands represent between-fish variation rather than measurement uncertainty. Group sample sizes for farmed/sea-caught fish were as follows: head, 87/167; eye, 85/165; pectoral fin, 87/169; dorsal region, 87/171; abdominal region, 87/170; and caudal fin, 87/171, respectively.

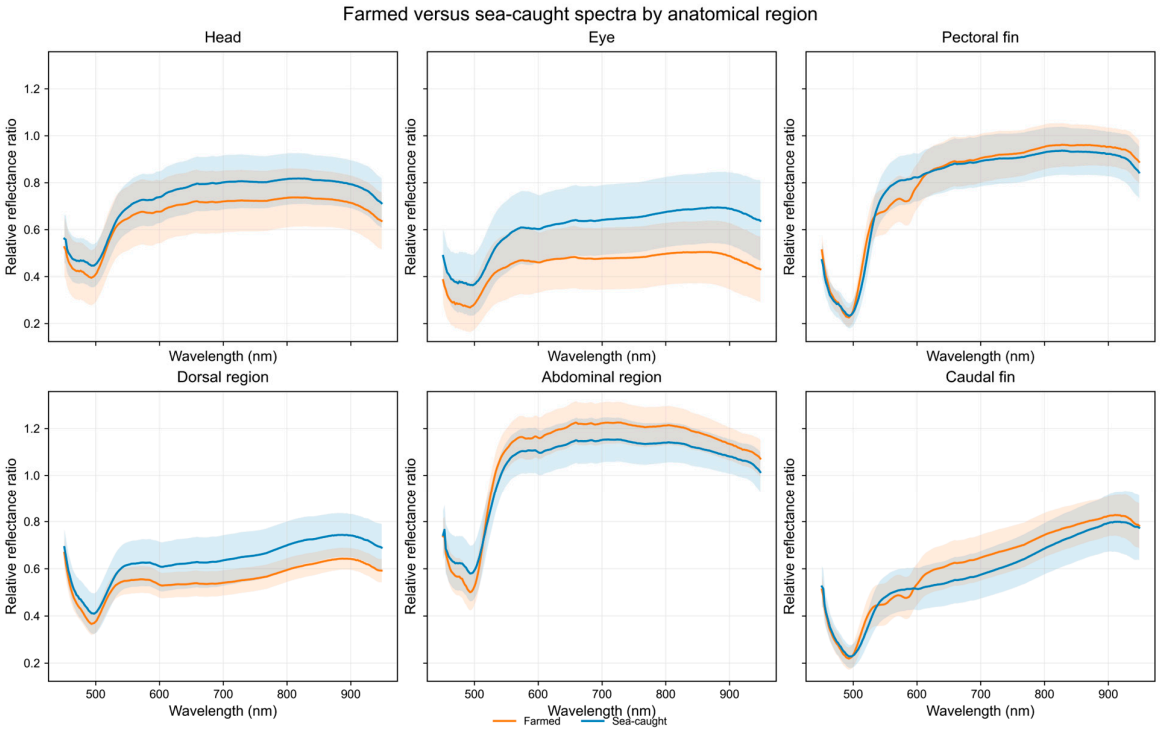


Figure 10. Farmed and sea-caught group mean relative reflectance-ratio spectra with ±1 SD shading for six anatomical regions over 450–950 nm. Orange denotes farmed fish, and blue denotes sea-caught fish. Exact fish counts are reported in Section 3.3; all panels use a common vertical scale.

The head region encompasses the snout, the external surface of the head, and the area adjacent to the operculum. Because of its complex local morphology, this region is more likely to be affected by posture, surface reflection, and differences in tissue boundaries, resulting in relatively obvious spectral fluctuations. The eye region is small in area and has strong curved-surface reflection and local pigmentation features. As a result, its

mean spectrum is more susceptible to segmentation boundaries and a small number of abnormal pixels.

In contrast, the abdominal region and the pectoral fin show more continuous curve patterns within the major wavelength range. Although their relative reflectance-ratio magnitudes are relatively high, the overall trends are stable. The abdominal region's pattern forms a broad plateau of high relative reflectance ratios within 600–850 nm, suggesting relatively stable relative reflectance-ratio characteristics in this region. The pectoral fin's pattern exhibits a distinct absorption valley in the short-wavelength region, followed by a rapid increase, resulting in a clearly defined spectral pattern. For the caudal fin, the standard deviation gradually increases in the near-infrared region. This may be related to its thinner tissue, prominent edge structure, and differences in the degree of caudal fin extension among individuals.

These spectra show region-dependent mean levels and between-fish variability. Region-specific analysis enabled source-associated patterns to be examined separately by anatomical region. Because no matched whole-fish mean-spectrum baseline was available, no conclusions about superiority over whole-fish analysis can be drawn.

3.4. Source-Associated Spectral Differences Across Anatomical Regions

Figure 10 compares the mean relative reflectance-ratio spectra of sea-caught and farmed fish across six anatomical regions. Difference patterns vary by anatomical region; this descriptive result indicates heterogeneous source associations rather than a uniform whole-fish shift.

Sea-caught fish had higher mean relative reflectance ratios in the head, eye, and dorsal regions across broad wavelength intervals. The eye showed the largest visible separation, although its small area and curved surface made it sensitive to reflection and mask-boundary variation. These observations indicate source-associated patterns within this cohort and do not identify their biological cause.

The farmed group had higher mean relative reflectance ratios in the abdominal region and at selected pectoral and caudal fin wavelengths. These patterns may also reflect uncontrolled differences in tissue condition, hydration, surface condition, handling, or acquisition batch; no causal mechanism was tested.

Pectoral fin differences change sign across wavelengths, whereas the pattern of the caudal fin tended to be higher in farmed fish after 600 nm. The corresponding standardized effects, confidence intervals, and multiplicity-adjusted tests are reported in Section 3.5.

Overall, the direction and magnitude of the sea-caught versus farmed contrasts varied among anatomical regions and wavelengths. The results therefore describe source-associated spectral differences within this cohort rather than a single causal effect of collection source.

3.5. Difference Spectra and Effect-Size Analysis Between Source Types

Fish-level wavelength-wise analysis identified region-dependent standardized differences (Figure 11 and Table 3). After Benjamini–Hochberg correction, 231 of 246 wavelengths were significant for the head, 246 for the eye, 97 for the pectoral fin, 246 for the dorsal region, 239 for the abdominal region, and 189 for the caudal fin. These counts reflect correlated spectral bands and should be interpreted together with effect magnitude and uncertainty, rather than as independent discoveries.

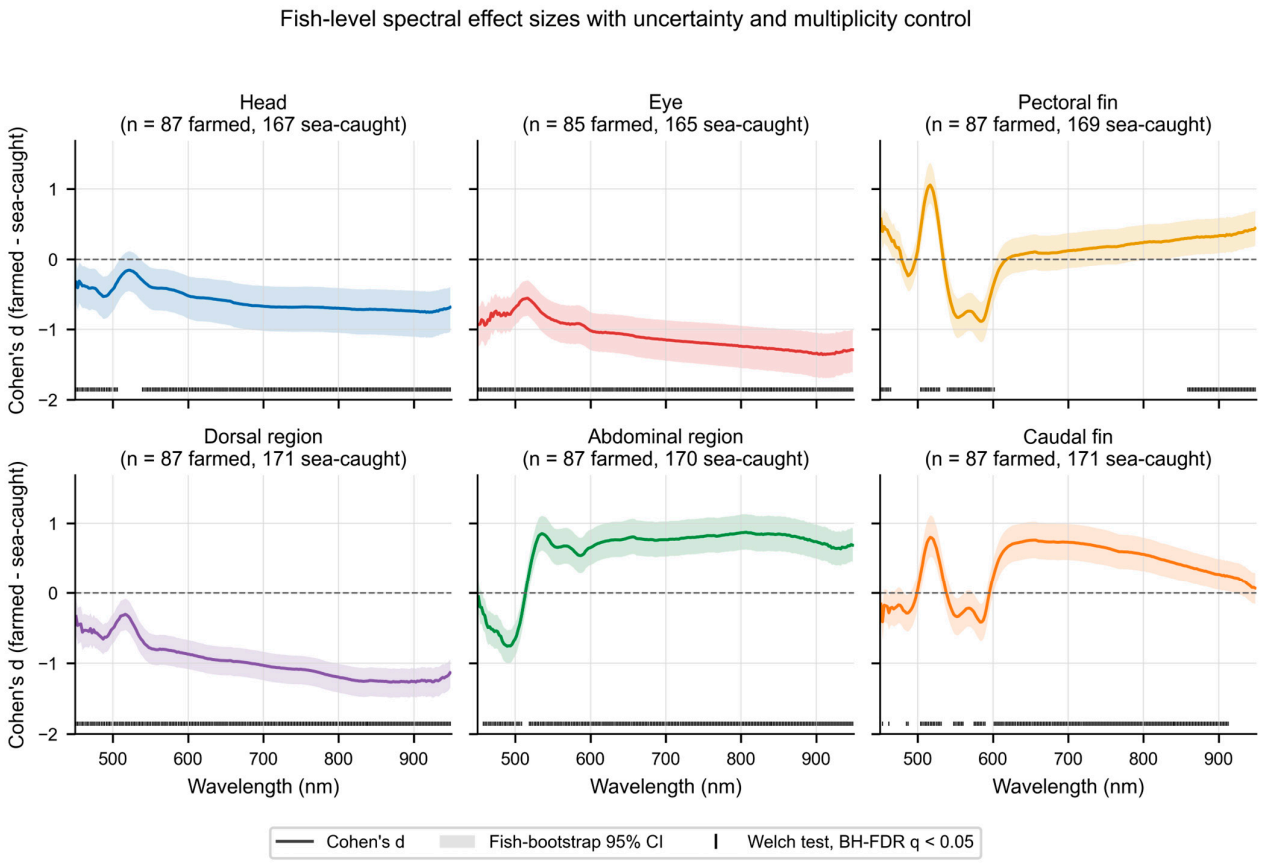


Figure 11. Fish-level Cohen's d for farmed-minus-sea-caught relative reflectance ratios over 450–950 nm. Lines show point estimates; shaded areas show stratified fish-bootstrap 95% confidence intervals (2000 resamples); bottom tick marks identify wavelengths with Benjamini–Hochberg adjusted *p*-values (q) < 0.05 within each anatomical region. Positive values indicate higher ratios in farmed fish, and negative values indicate higher ratios in sea-caught fish. All panels use a common vertical scale.

Table 3. Fish-level wavelength-wise source contrasts by anatomical region.

Anatomical Region	Fish n (F/SC)	FDR-Significant Bands/246	Peak |d| Wavelength (nm)	Signed d at Peak (Bootstrap 95% CI)	Higher-Ratio Group
Head	87/167	231/246	916.58	−0.756 (−1.118 to −0.461)	Sea-caught
Eye	85/165	246/246	908.65	−1.359 (−1.693 to −1.060)	Sea-caught
Pectoral fin	87/169	97/246	516.49	1.055 (0.798 to 1.376)	Farmed
Dorsal region	87/171	246/246	892.79	−1.266 (−1.483 to −1.078)	Sea-caught
Abdominal region	87/170	239/246	805.39	0.872 (0.630 to 1.132)	Farmed
Caudal fin	87/171	189/246	516.49	0.800 (0.526 to 1.115)	Farmed

The largest absolute effects occurred at 916.58 nm for the head (d = −0.756; 95% CI, −1.118 to −0.461), at 908.65 nm for the eye (d = −1.359; 95% CI, −1.693 to −1.060), and at 892.79 nm for the dorsal region (d = −1.266; 95% CI, −1.483 to −1.078). Negative values indicated higher relative reflectance ratios in sea-caught fish. The abdominal region had a

positive maximum at 805.39 nm (d = 0.872; 95% CI, 0.630–1.132), whereas the pectoral and caudal fins had positive maxima at 516.49 nm (d = 1.055 and 0.800, respectively), indicating higher ratios in farmed fish at those wavelengths.

The wavelength-wise contrasts describe association within the present cohort. They do not establish causal biological mechanisms, nor were the peak wavelengths selected as model features before cross-validation. Predictive performance was evaluated independently from these descriptive contrasts using the grouped procedures in Section 2.6.7.

Cohen's d was calculated as farmed minus sea-caught. Two-sided Welch's *t*-tests were corrected within each anatomical region using the Benjamini–Hochberg procedure; reported q values are adjusted *p*-values. Confidence intervals used 2000 stratified fish-level bootstrap resamples.

The univariate mean-difference and effect-size analyses identified pronounced source-related spectral contrasts in the eye, dorsal region, and head. These results describe the magnitude and direction of wavelength-specific differences, rather than a definitive ranking of predictive performance. The multivariate classification analysis reported in Section 3.7 provides the corresponding quantitative assessment of diagnostic performance for each region and for the combined model.

3.6. Principal Component Analysis Results

To visualize the distribution of different anatomical regions and samples in the overall spectral feature space, principal component analysis was performed on the selected spectral data. As shown in Figure 12, the first two principal components explained a relatively large proportion of spectral variation. The cumulative explained variance of PC1 and PC2 for the overall spectral dataset was high, indicating a strong low-dimensional structure in the original high-dimensional spectra.

In the anatomical-region score plot (Figure 12a), abdominal spectra are concentrated mainly toward negative PC1 values, whereas caudal fin spectra are more frequent toward positive PC1 values. The remaining regions overlap to varying degrees. Black x symbols mark region centroids, and the colored arrows show representative wavelength loading vectors. The wavelength-dependent PC1 and PC2 loading profiles are shown in Figure 12b.

The source-colored score plot (Figure 12c) shows overlap between sea-caught and farmed fish. Because spectra from all six anatomical regions are included, anatomical-region variation can dominate collection-source-associated variation. The eye-only panel (Figure 12d) shows a separation tendency but retains substantial overlap.

PCA was used only for visualization. It did not define the classification models or establish a diagnostic boundary; fish-grouped predictive results are reported separately in Section 3.7.

Taken together, the spectra show anatomical-region and collection-source associations in this cohort. PCA was descriptive and did not provide a validated classification boundary. Quantitative discrimination was therefore assessed using fish-grouped models, while conclusions were restricted to internal validation.

3.7. Internal Fish-Level Sea-Caught Versus Farmed Collection-Source Classification

Fish-level out-of-fold predictions from internal grouped cross-validation showed high collection-source discrimination within the available cohort. For logistic regression, the pectoral fin, the abdominal region, and the caudal fin achieved accuracy ratees of 0.996, 0.988, and 0.992, respectively. The combined six-region logistic-regression model achieved an accuracy of 0.996 (95% CI, 0.988–1.000), a balanced accuracy of 0.997 (95% CI, 0.991–1.000), an F1-score of 0.997 (95% CI, 0.991–1.000), and an AUC of 1.000 (95% CI, 1.000–1.000).

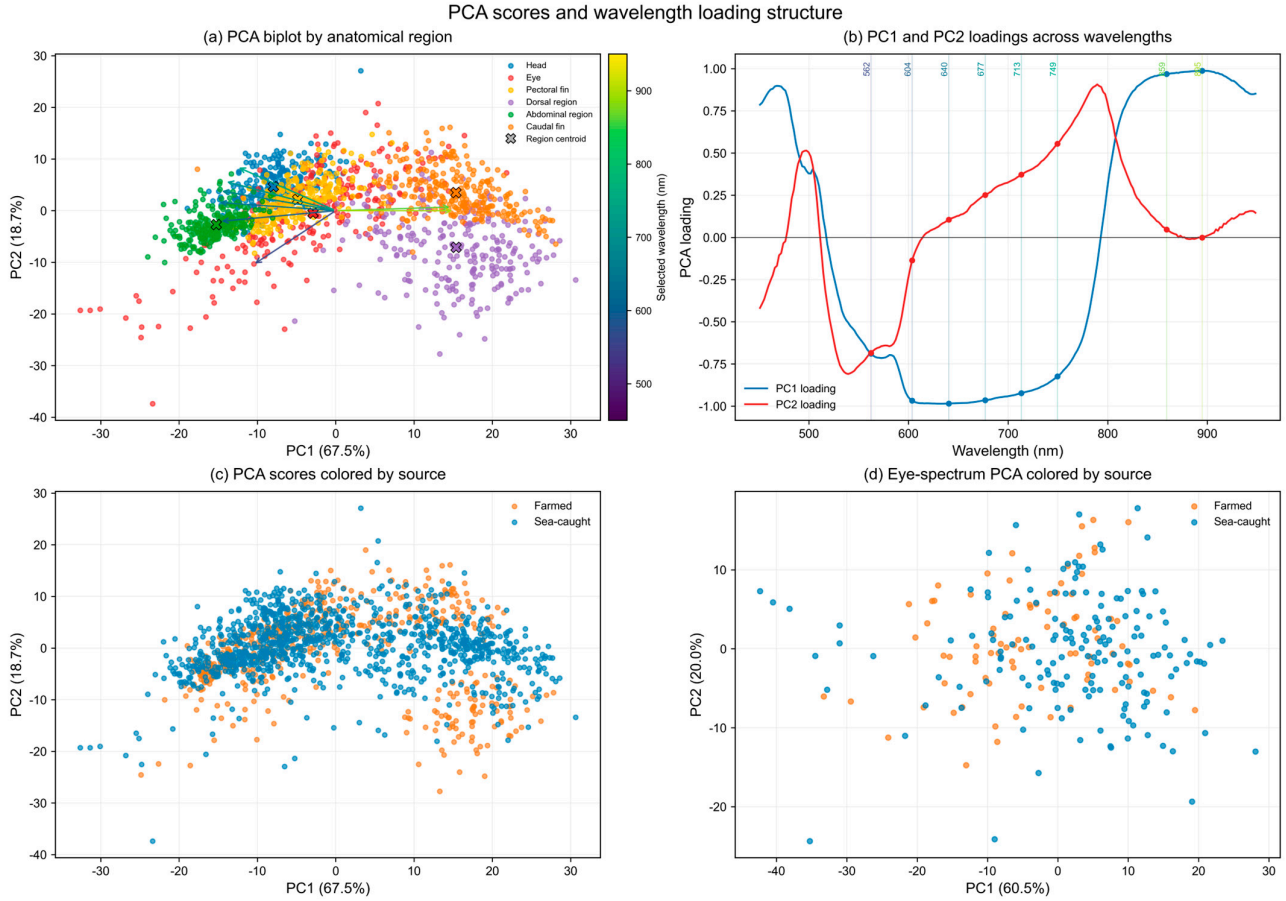


Figure 12. Principal-component analysis of SNV-preprocessed spectra over 450–950 nm. Panel (**a**) shows the PCA score distribution colored by anatomical region; black × symbols indicate region centroids, and the arrows represent selected wavelength loading vectors colored according to wavelength. Panel (**b**) shows the wavelength-dependent loading profiles of PC1 and PC2, illustrating the contribution of individual wavelengths to the two principal components. Panel (**c**) shows PCA scores colored by collection-source group (sea-caught versus farmed). Panel (**d**) shows the PCA score distribution for the eye region only, colored by collection-source group. Percentages shown on the PC axes indicate the proportion of variance explained by each principal component.

Logistic-regression AUC values ranged from 0.985 to 1.000 across the six individual anatomical regions, with the head and the eye yielding AUC values of 0.985 and 0.989, respectively. Random-forest models also showed substantial discriminatory performance, although their AUC values were generally lower than those of logistic regression. Random-forest AUC values ranged from 0.867 for the eye to 0.973 for the pectoral fin, while the combined six-region random-forest model achieved an AUC of 0.973. Figure 13 directly compares the fish-level AUC values and stratified bootstrap 95% confidence intervals of the logistic-regression and random-forest models across the six anatomical regions and the combined six-region model.

Complete model-specific performance metrics are reported in Table 4 for logistic regression and Table 5 for random forest. Figure 14 presents the fish-level receiver operating characteristic curves for the logistic-regression models. Figures 15 and 16 further present the corresponding fish-level confusion matrices for logistic regression and random forest, respectively, allowing the classification patterns and class-specific errors of the two modeling approaches to be examined across individual anatomical regions and the combined six-region model.

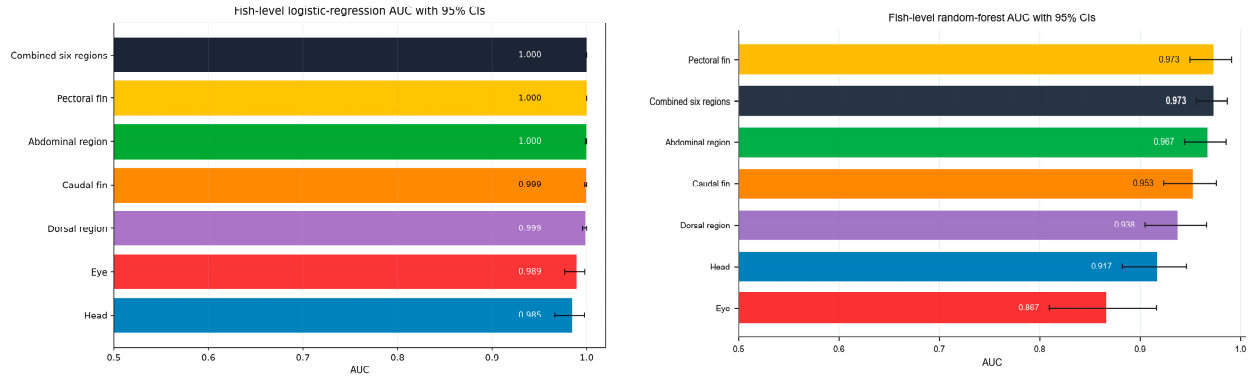


Figure 13. Fish-level AUC values and stratified bootstrap 95% confidence intervals for collection-source discrimination using logistic-regression and random-forest models across six anatomical regions and the combined six-region model.

Table 4. Internal fish-level collection-source discrimination performance of logistic-regression models. Values are point estimates with stratified fish-bootstrap 95% confidence intervals.

Region	Fish n (F/SC)	Accuracy	Sensitivity	Specificity	Balanced Accuracy	F1-Score	AUC
Head	254 (87/167)	0.949 (0.921–0.972)	0.946 (0.910–0.976)	0.954 (0.908–0.989)	0.950 (0.921–0.976)	0.960 (0.938–0.979)	0.985 (0.966–0.998)
Eye	250 (85/165)	0.952 (0.924–0.976)	0.945 (0.909–0.976)	0.965 (0.918–1.000)	0.955 (0.926–0.979)	0.963 (0.941–0.982)	0.989 (0.977–0.998)
Pectoral fin	256 (87/169)	0.996 (0.988–1.000)	0.994 (0.982–1.000)	1.000 (1.000–1.000)	0.997 (0.991–1.000)	0.997 (0.991–1.000)	1.000 (1.000–1.000)
Dorsal region	258 (87/171)	0.961 (0.938–0.984)	0.942 (0.906–0.977)	1.000 (1.000–1.000)	0.971 (0.953–0.988)	0.970 (0.951–0.988)	0.999 (0.996–1.000)
Abdominal region	257 (87/170)	0.988 (0.973–1.000)	0.988 (0.971–1.000)	0.989 (0.966–1.000)	0.988 (0.971–1.000)	0.991 (0.979–1.000)	1.000 (0.999–1.000)
Caudal fin	258 (87/171)	0.992 (0.981–1.000)	0.994 (0.982–1.000)	0.989 (0.966–1.000)	0.991 (0.977–1.000)	0.994 (0.985–1.000)	0.999 (0.998–1.000)
Combined six regions	250 (85/165)	0.996 (0.988–1.000)	0.994 (0.982–1.000)	1.000 (1.000–1.000)	0.997 (0.991–1.000)	0.997 (0.991–1.000)	1.000 (1.000–1.000)

Sea-caught fish were the positive class. Sensitivity denotes sea-caught recall, and specificity denotes farmed recall. All predictions were fish-level out-of-fold predictions from five-fold grouped cross-validation.

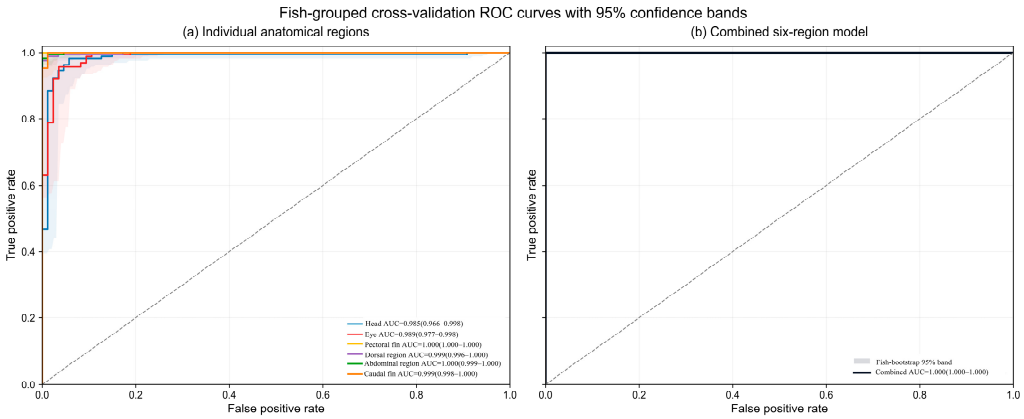


Figure 14. Internal fish-level grouped-cross-validation ROC curves for logistic-regression collection-source discrimination. The combined six-region model includes a stratified fish-bootstrap 95% confidence band.

Table 5. Internal fish-level collection-source discrimination performance of random-forest models. Values are point estimates with stratified fish-bootstrap 95% confidence intervals.

Region	Fish n (F/SC)	Accuracy	Sensitivity	Specificity	Balanced Accuracy	F1-Score	AUC
Head	254 (87/167)	0.839 (0.795–0.882)	0.874 (0.826–0.922)	0.770 (0.678–0.851)	0.822 (0.771–0.872)	0.877 (0.841–0.910)	0.917 (0.882–0.946)
Eye	250 (85/165)	0.844 (0.796–0.888)	0.897 (0.848–0.939)	0.741 (0.647–0.835)	0.819 (0.763–0.873)	0.884 (0.848–0.917)	0.867 (0.810–0.916)
Pectoral fin	256 (87/169)	0.945 (0.918–0.973)	0.970 (0.941–0.994)	0.897 (0.828–0.954)	0.933 (0.896–0.968)	0.959 (0.938–0.979)	0.973 (0.950–0.991)
Dorsal region	258 (87/171)	0.895 (0.857–0.930)	0.918 (0.871–0.953)	0.851 (0.770–0.920)	0.884 (0.838–0.925)	0.921 (0.890–0.948)	0.938 (0.905–0.966)
Abdominal region	257 (87/170)	0.899 (0.864–0.934)	0.953 (0.918–0.982)	0.793 (0.701–0.874)	0.873 (0.827–0.916)	0.926 (0.900–0.951)	0.967 (0.944–0.986)
Caudal fin	258 (87/171)	0.911 (0.876–0.942)	0.959 (0.930–0.988)	0.816 (0.724–0.897)	0.888 (0.842–0.928)	0.934 (0.909–0.957)	0.953 (0.924–0.976)
Combined six regions	250 (85/165)	0.912 (0.876–0.944)	0.952 (0.921–0.982)	0.835 (0.753–0.906)	0.893 (0.849–0.932)	0.935 (0.908–0.958)	0.973 (0.956–0.987)

Sea-caught fish were the positive class. Sensitivity denotes sea-caught recall, and specificity denotes farmed recall. All predictions were fish-level out-of-fold predictions from five-fold grouped cross-validation.

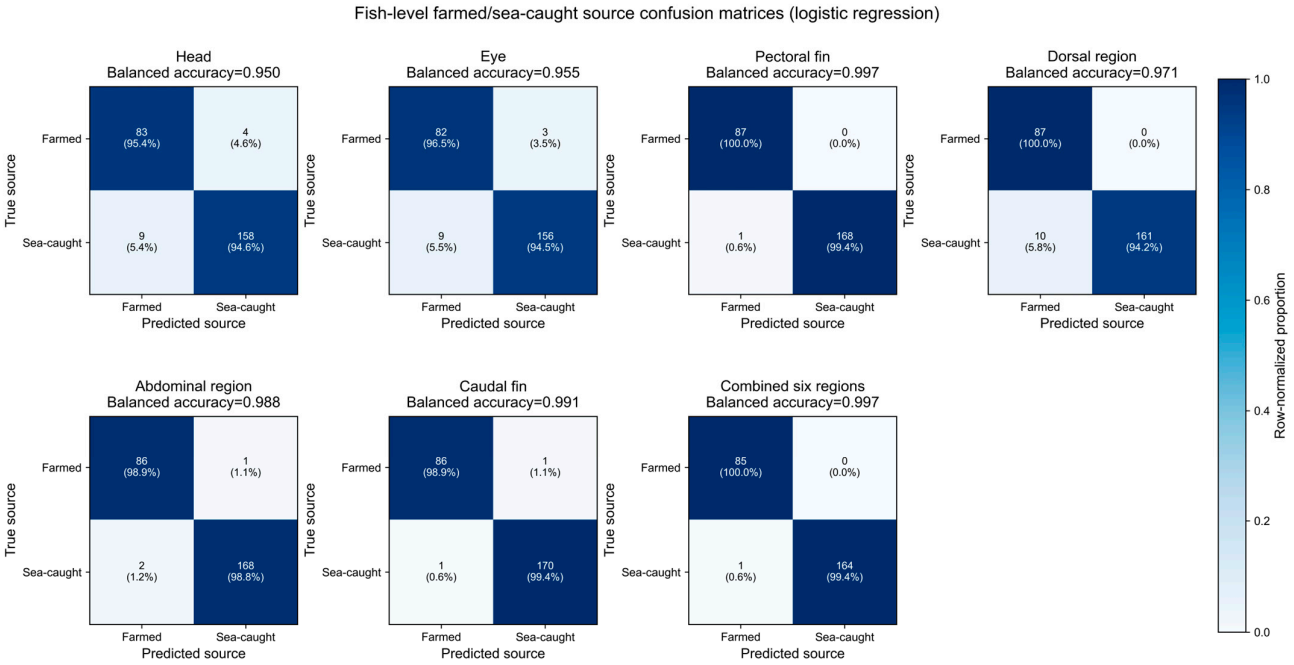


Figure 15. Internal fish-level confusion matrices for logistic-regression collection-source discrimination using each anatomical region and the combined six-region model. Sea-caught fish are the positive class.

In the repeated sensitivity analysis of the combined six-region logistic-regression model, 10 repeated five-fold fish-grouped cross-validations yielded a mean accuracy of 0.995 (SD, 0.002; range, 0.992–0.996), with an AUC of 1.000 in every repeat. In the 200-permutation fish-level label test, the observed AUC was 1.000, whereas the mean null AUC was 0.502 (SD, 0.052), with $p = 0.005$. These supplementary analyses support the internal robustness of the observed discrimination performance within the present cohort;

however, they do not constitute external validation, and no independent external cohort was available.

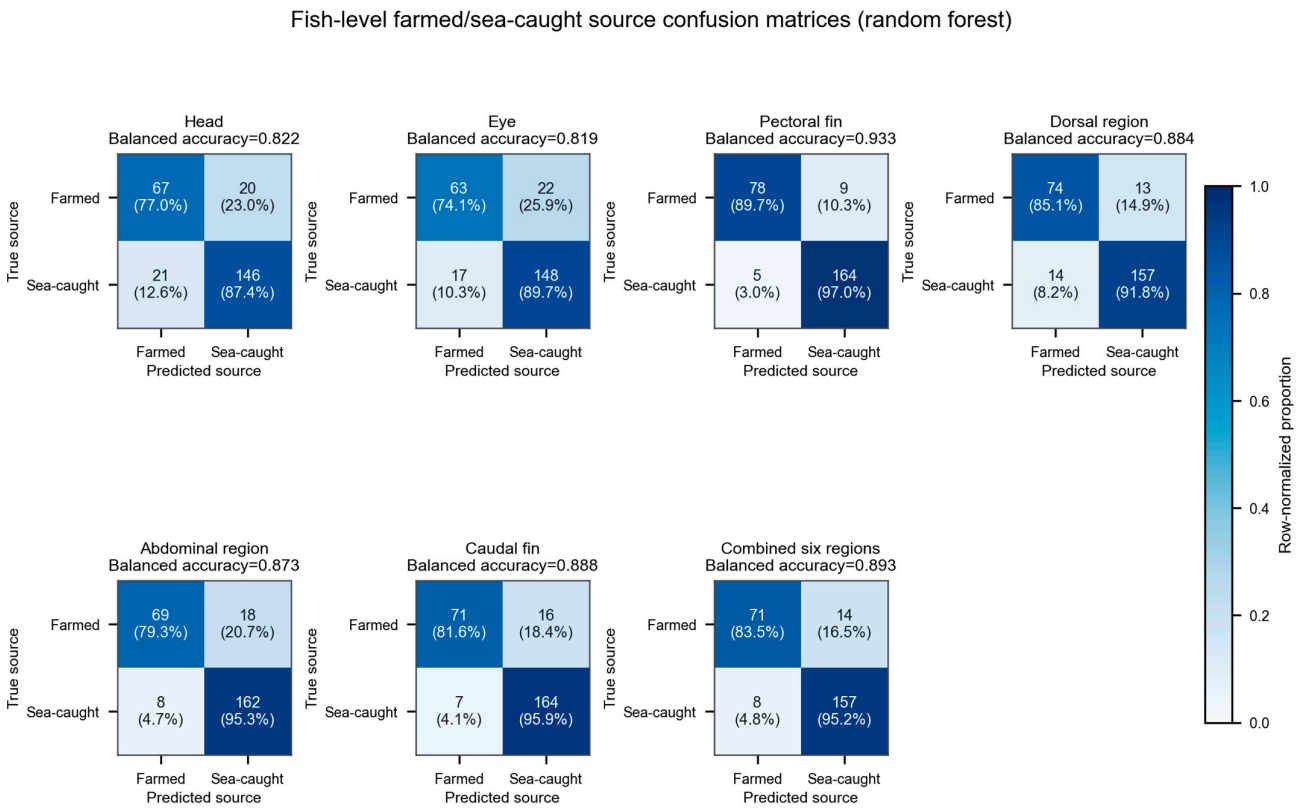


Figure 16. Fish-level confusion matrices for random-forest collection-source discrimination using six anatomical regions and the combined six-region model.

4. Discussion

4.1. Interpretation of Source-Associated Spectral Differences

The observed spectra differed by anatomical region and collection-source label, but these associations cannot be attributed causally to collection source. Age, sex, season, geographic origin, feed history, body condition, capture conditions, storage duration, surface moisture, and acquisition batch were not recorded comprehensively and could not be included in reliable covariate adjustment. Pigmentation, tissue structure, handling, and unmeasured acquisition factors may have therefore contributed to the observed source-associated spectral differences.

Body coloration has previously been associated with sea-caught and farmed large yellow croaker [31]. In the present cohort, higher relative reflectance ratios in sea-caught head, eye, and dorsal spectra were associated with the collection-source labels. The design cannot distinguish pigmentation, scale structure, tissue condition, handling, or acquisition effects.

The abdominal region showed the opposite direction, with higher relative reflectance ratios in farmed fish at several wavelengths. This observation is reported as a source-associated difference. Explanations involving feed, activity, tissue composition, hydration, or body condition remain hypotheses because the corresponding covariates and direct chemical or histological measurements were unavailable.

The eye region showed pronounced source-associated differences but is sensitive to curved-surface reflection, local pigmentation, segmentation boundaries, and noise. The results support its contribution to within-cohort discrimination, not a causal interpretation or standalone authentication claim.

4.2. Interpretive Value and Current Limits of Anatomical-Region Analysis

Anatomical-region extraction enabled the spectral characteristics of six predefined regions to be examined separately and supported comparison among individual-region models and a combined six-region model.

A matched whole-fish baseline could not be reconstructed reliably because a compatible whole-fish mask and mean spectrum were not retained for every fish. Applying the same preprocessing, folds, and classifiers would require reprocessing the original cubes.

Accordingly, all comparative claims that regional spectra outperform whole-fish averaging, prevent information loss, or exploit spatial information more effectively have been removed. The present evidence supports only examination of separate anatomical regions and comparison of individual-region models with a combined-region model.

YOLO11n-seg automated the extraction of predefined anatomical masks, but segmentation quality varied at stricter overlap thresholds. Future comparison with manual ROIs and whole-fish masks should use identical fish-level folds and paired statistical testing.

4.3. Comparison with Related Hyperspectral and Fish-Vision Studies

The related literature spans hyperspectral seafood assessment and fish computer vision. These studies provide context for the components of the workflow but do not validate sea-caught versus farmed collection-source discrimination in the present cohort.

No independent study with the same species, six anatomical masks, hyperspectral acquisition, collection-source labels, and fish-grouped classification design was identified. Table 6 therefore provides contextual, not head-to-head, comparison. The present validation-set mask mAP@0.5 and mAP@0.5–0.95 were 0.972 and 0.669; comparison with differently defined datasets cannot establish superiority or generalizability.

Table 6. Contextual comparison with independent hyperspectral and fish-vision studies.

Study	Independent Dataset or Task	Reported Scale or Performance	Relationship to the Present Study
Yao et al. [5]	Large yellow croaker whole-fish and anatomical-contour segmentation for morphometry	P 0.9853; R 0.9924; mAP@0.5 0.9897; mAP@0.5–0.95 0.8324	Closest numerical segmentation comparator, but it used visible images and a different target definition
Garcia-d'Urso et al. [15]	DeepFish market-tray dataset for fish instance segmentation, species classification, and size estimation	1291 labeled images; 7339 specimens; 59 species	Supports pixel-wise fish segmentation and biological independence but does not segment anatomical regions or use hyperspectral data
Mehrab et al. [20]	Fish-Vista benchmark for species classification, trait identification, and trait segmentation	69,269 images; 4316 species	Establishes trait segmentation and small-object/OOD challenges, but not source classification from hyperspectral spectra
Xu et al. [32]	Hyperspectral and computer-vision differentiation of organic and conventional farmed salmon	Visible HSI: 400–1000 nm; SWIR HSI: 897–1753 nm	Closest independent production-system classification study; different species, fillet target, labels, and validation design
Present study	Seven-class mask segmentation in RGB previews aligned with hyperspectral cubes	P 0.969; R 0.976; mAP@0.5 0.972; mAP@0.5–0.95 0.669	Six anatomical regions plus the white reference board; metrics are internal validation estimates

P, precision; R, recall; OOD, out of distribution. Present-study aggregate mask metrics were calculated on the 20-image validation set (10 sea-caught and 10 farmed; 140 annotated instances). Because datasets and target definitions differ, Table 6 provides context rather than a head-to-head benchmark.

The per-class values in Table 2 describe the separate 10-image test split from the same source dataset. They are useful for identifying weaker anatomical classes but do not constitute an independent external evaluation.

The methodological contribution is the integration of anatomical-region segmentation, relative white-reference normalization, and internal fish-level classification with uncertainty reporting. This study does not establish superiority over whole-fish analysis or independent provenance authentication. Anatomical-region masks were mapped to the hyperspectral data to extract relative reflectance-ratio spectra in a standardized manner. This integration supports automated examination of predefined anatomical regions within the current dataset; it does not establish causal mechanisms or superiority over a matched whole-fish workflow.

PCA and effect-size analyses showed that spectral distributions were associated with anatomical regions. These descriptive results support retaining anatomical-region labels in the analysis but do not demonstrate that region-specific features outperform a whole-fish baseline.

4.4. Potential Application of Collection-Source Discrimination

The combined workflow showed preliminary potential for sea-caught versus farmed collection-source discrimination under the controlled conditions and operational labels used here. Translation to provenance or traceability authentication would require independently verified labels, external cohorts, standard white-and-dark calibration, and prospective evaluation across farms, capture locations, seasons, and collection periods.

The region-specific results may guide future sensor simplification and band-selection studies. They do not establish that partial scanning is sufficient, because the present analysis began from full hyperspectral acquisitions and did not compare acquisition strategies prospectively. The workflow may be evaluated in future aquatic-product studies using prospectively recorded covariates and independently verified outcomes. Such extensions should not be inferred from the current cohort.

4.5. Limitations and Future Research Directions

This study has several limitations. The sea-caught and farmed groups were operational collection-source labels assigned from the original capture or cage-culture channels. Complete per-fish traceability records were not retained and were not reconstructed, and no independent genetic, chemical, documentary, or traceability verification was performed. Age, sex, season, geographic origin, feed history, body condition, capture conditions, storage duration, surface moisture, and acquisition batch were not completely recorded. Reliable matching, stratification, or multivariable covariate adjustment could therefore not be performed, and the reported differences may reflect uncontrolled confounding.

The classification results are internal fish-level validation estimates. Grouped folds prevented data from the same fish from crossing training and validation portions, and preprocessing was fitted within training folds, but no independent external cohort from different farms, capture locations, seasons, nor collection periods was available. Repeated grouped cross-validation and permutation testing support internal robustness only. The 10-image YOLO test split was held out from model selection and had non-overlapping linked fish IDs, but it came from the same source dataset and should not be interpreted as a genuine independent external evaluation. Larger independently collected and annotated cohorts are required. Relative white-reference normalization did not subtract dark current or other additive detector effects, and repeatability was not tested across settings, sessions, or devices. A matched whole-fish baseline was unavailable. Future work should use standard

white-and-dark calibration, prospectively record confounders, compare matched whole-fish and anatomical-region models, and evaluate independently verified multi-origin cohorts.

5. Conclusions

This study developed a fish-level analytical workflow integrating YOLO11n-seg-based anatomical-region segmentation with visible–near-infrared hyperspectral imaging to extract relative reflectance ratios from six anatomical regions of large yellow croaker. Source-associated spectral differences were observed across the analyzed regions, indicating that different anatomical regions contain locally distinct spectral information related to the collection-source groups. Logistic-regression models showed high internal fish-level cross-validation performance for discriminating sea-caught and farmed collection-source groups. Among the evaluated models, the combined six-region logistic-regression model achieved an internally cross-validated accuracy of 0.996 (95% CI, 0.988–1.000) and an AUC of 1.000 (95% CI, 1.000–1.000). These findings demonstrate the feasibility of combining anatomical-region segmentation with region-specific hyperspectral features for collection-source discrimination within the present cohort and suggest that localized spectral information may provide an interpretable basis for characterizing differences between the two collection-source groups.

The present findings should, however, be interpreted within the scope of internal validation. Future studies should assess the generalizability of the proposed approach using independent external cohorts collected from different farms, capture locations, seasons, and acquisition periods. Independently verified provenance labels and more complete records of potential confounding variables, including age, sex, geographic origin, feed history, body condition, capture conditions, storage duration, surface moisture, and acquisition batch, should also be incorporated to enable more rigorous evaluation and covariate adjustment. In addition, standardized white- and dark-reference calibration procedures, together with calibration-repeatability assessments, are needed to improve measurement comparability and evaluate the stability of the spectral acquisition process. Matched whole-fish spectral analyses should further be included to determine whether region-specific spectral features provide additional discriminatory information beyond whole-fish spectra. With these methodological improvements and independent validation, the proposed workflow could provide a stronger and more transferable basis for future non-destructive assessment of large yellow croaker collection source.

Author Contributions: Conceptualization, X.A., S.Z. and Q.G.; methodology, X.A., J.W. and S.Z.; software, X.A. and J.W.; validation, X.A., J.W. and B.W.; formal analysis, X.A. and J.W.; investigation, X.A., N.L. and B.W.; resources, S.Z. and Q.G.; data curation, X.A., J.W. and N.L.; writing—original draft preparation, X.A.; writing—review and editing, J.W., S.Z., N.L., B.W. and Q.G.; visualization, X.A. and J.W.; supervision, S.Z. and Q.G.; project administration, S.Z. and Q.G.; funding acquisition, S.Z. and Q.G. All authors have read and agreed to the published version of the manuscript.

Funding: This research study was funded by the National Key Research and Development Program of China (2022YFD2401103). the National Key Research and Development Program of China, grant number (2023YFD2401400); the Central Public-interest Scientific Institution Basal Research Fund, CAFS (2026XT0203).

Institutional Review Board Statement: Ethical review and approval were waived because all fish samples were obtained post mortem through commercial capture or aquaculture collection channels; no live-animal experiment, invasive treatment, or animal-welfare intervention was performed.

Data Availability Statement: The original contributions presented in this study are included in the article. Further inquiries can be directed to the corresponding authors.

Acknowledgments: The authors gratefully acknowledge the valuable assistance and support provided by all co-authors.

Conflicts of Interest: The authors declare no conflicts of interest.

References

1. Liu, M.; De Mitcheson, Y.S. Profile of a fishery collapse: Why mariculture failed to save the large yellow croaker. *Fish Fish.* **2008**, *9*, 219–242. [CrossRef]
2. Li, X.; Li, B.; Chen, N.; Huang, X.; Hua, X.; Leng, X. A comparison study on flesh quality of large yellow croaker (*Larimichthys croceus*) cultured with three different modes. *J. Ocean Univ. China* **2017**, *16*, 1187–1194. [CrossRef]
3. Ma, R.; Meng, Y.; Zhang, W.; Mai, K. Comparative study on the organoleptic quality of wild and farmed large yellow croaker *Larimichthys crocea*. *J. Oceanol. Limnol.* **2020**, *38*, 260–274. [CrossRef]
4. Xu, K.; Wang, J.; Zhou, Y.; Zhu, K.; Fang, G.; Wang, H.; Zeng, J. A group identification method based on trace element levels of muscle tissue: A case study for Oplegnathus fasciatus in the Northern Zhejiang Waters. *Front. Mar. Sci.* **2025**, *12*, 1627012. [CrossRef]
5. Yao, Y.; Guo, Q.; Zhang, S.; Wu, J.; Chen, T.; Lin, N.; Wu, Z.; Zheng, H. Image-Based Analysis of Morphometric Differences Between Sea-Caught and Farmed Large Yellow Croaker (*Larimichthys crocea*). *Animals* **2026**, *16*, 601. [CrossRef] [PubMed]
6. Zion, B. The use of computer vision technologies in aquaculture—A review. *Comput. Electron. Agric.* **2012**, *88*, 125–132. [CrossRef]
7. Saberioon, M.; Gholizadeh, A.; Cisar, P.; Pautsina, A.; Urban, J. Application of machine vision systems in aquaculture with emphasis on fish: State-of-the-art and key issues. *Rev. Aquac.* **2017**, *9*, 369–387. [CrossRef]
8. Li, P.; Han, H.; Zhang, S.; Fang, H.; Fan, W.; Zhao, F.; Xu, C. Reviews on the development of digital intelligent fisheries technology in aquaculture. *Aquac. Int.* **2025**, *33*, 191. [CrossRef]
9. Yang, H.; Feng, Q.; Xia, S.; Wu, Z.; Zhang, Y. AI-driven aquaculture: A review of technological innovations and their sustainable impacts. *Artif. Intell. Agric.* **2025**, *15*, 508–525. [CrossRef]
10. Ai, X.; Zhang, S.; Yang, S.; Guo, A.; Wu, Z.; Fan, X.; Wu, Y.; Shi, Y. A Lightweight YOLO-PEGA-Based Method for Quantifying Fish Feeding Intensity. *Animals* **2026**, *16*, 432. [CrossRef] [PubMed]
11. Gu, X.; Zhang, S.; Ai, X.; Yang, S.; Wu, Z. GUM-compliant automatic fish morphometry via transformer-enhanced keypoint detection. *Measurement* **2026**, *282*, 122087. [CrossRef]
12. Han, X.; Zhang, S.; Cheng, T.; Yang, S.; Fan, M.; Lu, J.; Guo, A. FishSegNet-PRL: A Lightweight Model for High-Precision Fish Instance Segmentation and Feeding Intensity Quantification. *Fishes* **2025**, *10*, 630. [CrossRef]
13. Han, X.; Zhang, S.; Wang, Y.; Fang, H.; Peng, S.; Yang, S.; Wu, Z. Seedling Selection of the Large Yellow Croaker (*Larimichthys crocea*) for Sustainable Aquaculture: A Review. *Appl. Sci.* **2025**, *15*, 7307. [CrossRef]
14. Jiang, Z.; Bai, Y.; Li, N.; Chen, L.; Zhao, J.; Li, Y.; Zhou, T.; Xu, P. Genomic Approaches to Enhance Disease Resistance in Large Yellow Croaker: Recent Progress and Future Perspectives. *Rev. Aquac.* **2025**, *17*, e70084. [CrossRef]
15. Garcia-d'Urso, N.; Galan-Cuenca, A.; Perez-Sanchez, P.; Climent-Perez, P.; Fuster-Guillo, A.; Azorin-Lopez, J.; Saval-Calvo, M.; Guillen-Nieto, J.E.; Soler-Capdepon, G. The DeepFish computer vision dataset for fish instance segmentation, classification, and size estimation. *Sci. Data* **2022**, *9*, 287. [CrossRef]
16. Zhang, J.; Wang, S.; Zhang, S.; Li, J.; Sun, Y. Research on target detection and recognition algorithm of Eriocheir sinensis carapace. *Multimed. Tools Appl.* **2023**, *82*, 42527–42543. [CrossRef]
17. Wang, X.; Yu, H.; Zhang, C.; Liu, Z.; Luo, Z.; Chen, Y. An underwater image dataset for occlusion-aware fish instance segmentation. *Sci. Data* **2026**, *13*, 526. [CrossRef] [PubMed]
18. Wang, S.; Zhang, S.; Shi, Y.; Wu, Z.; Cheng, T. Integrated Laser Imaging for Fusiform Fish Measurement in Aquaculture. *Fishes* **2026**, *11*, 298. [CrossRef]
19. Feng, G.; Wang, H.; Chen, M.; Liu, Z. Accurate Segmentation of Tilapia Fish Body Parts Based on Deeplabv3+ for Advancing Phenotyping Applications. *Appl. Sci.* **2023**, *13*, 9635. [CrossRef]
20. Mehrab, K.S.; Maruf, M.; Daw, A.; Neog, A.; Manogaran, H.B.; Khurana, M.; Feng, Z.; Altintas, B.; Bakis, Y.; Campolongo, E.G.; et al. Fish-Vista: A Multi-Purpose Dataset for Understanding and Identification of Traits from Images. In Proceedings of the IEEE/CVF Conference on Computer Vision and Pattern Recognition, Nashville, TN, USA, 11–15 June 2025; pp. 24275–24285.
21. Yao, Y.; Qiao, G.; Zhang, S.; Wu, C.; Wu, Z.; Cheng, T.; Zheng, H. Research on Morphometric Methods for *Larimichthys crocea* Based on YOLOv11-CBAM X-Ray Imaging. *Fishes* **2025**, *10*, 641. [CrossRef]
22. Redmon, J.; Divvala, S.; Girshick, R.; Farhadi, A. You Only Look Once: Unified, Real-Time Object Detection. In Proceedings of the 2016 IEEE Conference on Computer Vision and Pattern Recognition (CVPR), Las Vegas, NV, USA, 27–30 June 2016; pp. 779–788.
23. Redmon, J.; Farhadi, A. YOLO9000: Better, Faster, Stronger. In Proceedings of the 2017 IEEE Conference on Computer Vision and Pattern Recognition (CVPR), Honolulu, HI, USA, 21–16 July 2017; pp. 7263–7271.
24. Redmon, J.; Farhadi, A. YOLOv3: An Incremental Improvement. *arXiv* **2018**, arXiv:1804.02767. [CrossRef]

25. Wang, C.-Y.; Bochkovskiy, A.; Liao, H.-Y.M. YOLOv7: Trainable Bag-of-Freebies Sets New State-of-the-Art for Real-Time Object Detectors. In Proceedings of the 2023 IEEE/CVF Conference on Computer Vision and Pattern Recognition (CVPR), Vancouver, BC, Canada, 18–22 June 2023; pp. 7464–7475.
26. Ultralytics. YOLO11 Model Documentation. Available online: https://docs.ultralytics.com/models/yolo11/ (accessed on 13 August 2026).
27. Ultralytics. Instance Segmentation Documentation. Available online: https://docs.ultralytics.com/tasks/segment/ (accessed on 13 August 2026).
28. Bolya, D.; Zhou, C.; Xiao, F.; Lee, Y.J. YOLACT++: Better Real-Time Instance Segmentation. *IEEE Trans. Pattern Anal. Mach. Intell.* **2022**, *44*, 1108–1121. [CrossRef] [PubMed]
29. He, K.; Gkioxari, G.; Dollár, P.; Girshick, R. Mask R-CNN. In Proceedings of the 2017 IEEE International Conference on Computer Vision (ICCV), Venice, Italy, 22–29 October 2017; pp. 2961–2969.
30. Cheng, B.; Misra, I.; Schwing, A.G.; Kirillov, A.; Girdhar, R. Masked-Attention Mask Transformer for Universal Image Segmentation. In Proceedings of the 2022 IEEE/CVF Conference on Computer Vision and Pattern Recognition (CVPR), New Orleans, LA, USA, 19–24 June 2022; pp. 1290–1299.
31. Yi, X.W.; Li, J.; Xu, W.; Zhang, Y.J.; Zhou, H.H.; Smith, A.A.; Zhang, W.B.; Mai, K.S. Effects of dietary xanthophylls/astaxanthin ratios on the growth and skin pigmentation of large yellow croaker *Larimichthys crocea* (Richardson, 1846). *J. Appl. Ichthyol.* **2015**, *31*, 780–786. [CrossRef]
32. Xu, J.-L.; Riccioli, C.; Sun, D.-W. Comparison of hyperspectral imaging and computer vision for automatic differentiation of organically and conventionally farmed salmon. *J. Food Eng.* **2017**, *196*, 170–182. [CrossRef]

Disclaimer/Publisher's Note: The statements, opinions and data contained in all publications are solely those of the individual author(s) and contributor(s) and not of MDPI and/or the editor(s). MDPI and/or the editor(s) disclaim responsibility for any injury to people or property resulting from any ideas, methods, instructions or products referred to in the content.